

A GENERAL DESIGN METHODOLOGY FOR YEAR-ROUND SOLAR-POWERED STRATOSPHERIC UAVS FROM LOW TO MIDDLE LATITUDES

Min Chang^{1,2}, Zhou Zhou¹, Rui Wang¹, Xiaoping Xu¹

¹ Science and Technology on UAV Laboratory, Northwestern Polytechnical University

² Xi'an Institute of Modern Control Technology

Keywords: *Solar-powered UAV, latitude, design methodology, energy performance*

Abstract

A design methodology for configuration sizing of solar-powered UAVs is established, which could be equally applied to all configurations capable of year-round operations in the stratosphere at low and middle latitudes. In general, the configurations are classified into two representative types—the conventional and the wing-sail. The wing-sail configuration employs sail tails that can rotate around individual roll axes to maximize solar energy absorption, and photovoltaic (PV) modules are coupled to the wing and only one side of each sail tail. The configuration sizes are treated as key design variables, including wingspan, aspect ratio of wing, and area ratio of sail tails to the wing.

The established methodology mainly contains two parts. The first part parameterizes energy absorption and energy consumption, mass components and aerodynamic efficiency. The second part employs an optimal approach to obtain a group of optimized solutions. Then, the methodology is applied to analyze conceptual parameters at different latitudes for both configurations. Finally, a solar powered stratospheric UAV concept of wing-sail configuration, PoXiao, is proposed for year-round operation at middle latitudes. Its energy performance is investigated to validate the operational altitude and latitude capabilities throughout a whole year and demonstrate the utility of the design methodology. The characteristics of stability and control for the wing-sail configuration is also preliminary analyzed.

1 General Introduction

The solar energy has attracted many researchers in the last 40 years due to its clearness and eternity for high altitude long endurance (HALE) unmanned aerial vehicles (UAV). Solar-powered UAVs show their superiorities in the civil or military fields. Higher altitude means wider covering area of interest and higher survivability, and longer endurance means more timely intelligence and information.

References[1-3] mainly focused on traditional design processes of solar-powered airplanes and validated the feasibility of solar-powered flight. Bailey[4] generally discussed component parameters determination, presented and analyzed a high-altitude solar-powered platform for a proposed mission. Steven[5] studied the energy characteristics for solar-powered flying wing, tandem wing and airship under the constraint of energy balance. Romeo[6, 7] carried out research activities on HALE platforms to achieve persistent operations for several months in the northern latitudes of $36^{\circ}\sim 45^{\circ}$ at the altitudes of 15~20 km in Europe. Noth[8] developed a conceptual design methodology, and successfully achieved continuous flight of 27 h by solar-powered Sky-Sailor near the summer solstice at the latitude of 44°N in 2008. Rizzo[9] proposed a mathematical model for conceptual design and compared 4 representative configurations based on energy characteristics. Comprehensively speaking, these design methodologies above are merely focused on continuous operation near

the equator or continuous flight for a single day or several weeks at higher latitudes when the solar radiation is rich, and are scarcely focused on year-round operation at higher latitudes. In the history of solar-powered flight, solar-powered Helios and Zephyr respectively produced records of absolute altitude of 29,531 m for 4 hours on August 13, 2001 in Hawaii (18°N) [10] and endurance of 336 hours from 15 km to 18 km in July 23, 2010 in Yuma (32°N) verified by Fédération Aéronautique Internationale. Their PV modules are both horizontally mounted only on their wings conventionally. With conceptual parameters of flying-wing Helios prototype (HP01) from Ref. [10], Fig. 1 shows its achievable persistent altitudes from low to middle latitudes throughout a whole year.

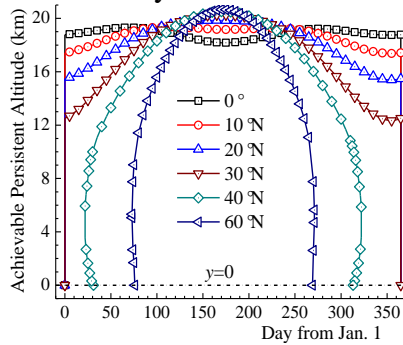


Fig. 1 Persistent altitude capability of the Helios prototype (HP01)

The HP01 could fly continuously within the region bounded by each curve and the sea level ($y = 0$). It is obvious that the HP01 could not maintain station keeping at high altitudes and higher latitudes during the winter months. It is due to the fact that both the solar elevation angle on average and the day length near winter decrease with increasing latitude, leading to the decreasing of the solar flux in the daytime projected on a surface disposed horizontally, i.e. on the wing [11, 12]. It is also the key reason why to date solar-powered UAVs with PV modules only mounted on the wing have limited operational values, especially at high altitudes and higher latitudes near winter.

Inspired by the solar collector “tracking” the Sun to minimize the angle of incidence of beam radiation on the surfaces with PV modules, Keidel [13] from Germany and Gerald [14] from the Boeing Company both innovatively

proposed the configurations which incorporated rotatable sun-trackers into solar-powered airplanes of conventional configuration to achieve longer flight duration at higher latitudes. However, they did not systematically present the methods for sizing the wing and non-horizontal sun-trackers. Ref. [15] also proves the superiorities of sun-trackers with variable orientations when applied to high-altitude solar-powered UAVs at wide latitudes.

In general, the configurations for solar-powered airplanes can be categorized into two representative types—the conventional and the wing-sail, as shown in Fig. 2. For the conventional, PV modules are mainly horizontally disposed on the wing. For the wing-sail, a portion of PV modules is horizontally disposed as the conventional, and the rest are mounted on the sail tails that can rotate around body axes. The conventional is a special case of the wing-sail when the total area of sail tails is zero, and the all-wing design like Helios with no fuselages and tails belongs to the conventional.

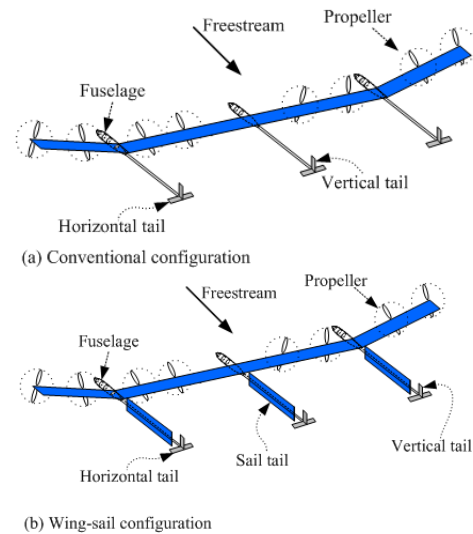


Fig. 2 Perspective views of exemplary embodiments of conventional and wing-sail configurations

Thus, this paper aims to define a mathematical model of design methodology for configuration sizing of solar-powered stratospheric UAVs for year-round mission requirements from low to middle latitudes. This design methodology is under the constraints that energy consumption is balanced by energy absorption within the daytime, the nighttime and a whole day of 24 hours. As to energy

absorption, power area density of PV modules is modeled, considerations including PV modules' orientation, thermodynamics of PV modules, propagation of solar radiation, flight direction, operational altitude, operational latitude, different seasons, etc. As to energy consumption, each mass component is parameterized and aerodynamic efficiency model based on configuration parameters is built. Besides, Quantum-Behaved Particle Swarm (QPSO) algorithm and Kriging surrogate model are employed to achieve an optimal group of configuration parameters efficiently. A fitness function of AR of wing, cruise velocity and payload weight fraction is defined to link the optimization and the QPSO algorithm. Finally, the established design methodology is put into applications. Firstly, the key conceptual parameters obtained by the design methodology for both configurations are compared from the equator to the latitude of 50°N. Secondly, a solar powered stratospheric UAV concept of wing-sail configuration, PoXiao, is designed at the latitude of 45°N. Then, the flight performance, power characteristics, and tracking angles of PoXiao concept on the summer solstice and the winter solstice are explored, and operational persistent altitude and payload power capabilities are further investigated at middle latitudes throughout a whole year. In addition, the impacts of the installation and the rotation of sail tails of the wing-sail configuration from a stability and control point of view are preliminary analyzed.

2 Basic Equations: Energy Balance and Mass Balance

Based on the potential application listed at the beginning, steady level flight acts as the single design point for solar-powered stratospheric UAVs as other HALE airplanes. The following study is only concentrated on level flight at constant altitude and storing the diurnal surplus of solar energy only in secondary batteries. The basic equations contain mass balance and energy balance.

Firstly, the mass balance means that the lifting force has to be equal to or higher than the total weight of every component constituting the

airplane. The solar-powered airplane does not change its weight in operation. In general, the total weight can be divided into eight parts. Equation (1) summarizes the total-weight buildup:

$$m_{\text{tot}} = m_{\text{pld}} + m_{\text{af}} + m_{\text{pm}} + m_{\text{mppt}} + m_{\text{bat}} + m_{\text{p}} + m_{\text{av}} + m_{\text{lg}} \quad (1)$$

Here m_{pld} , m_{af} , m_{pm} , m_{mppt} , m_{bat} , m_{p} , m_{av} and m_{lg} represent the mass of payload, airframe structure, PV modules, MPPT, secondary batteries, propulsion systems, avionics and landing gear, respectively.

Secondly, the energy balance means that the total energy collected from onboard PV modules must be equal to or higher than the electrical energy consumed for mission execution in a whole day of 24 hours. The relationship is defined by:

$$S_w K_{\text{pm}} (H_d + H_n) = P_{\text{tot}} [H_d + H_n / (\eta_c \eta_{\text{dc}})] \quad (2)$$

Here S_w donates the reference area of wing, K_{pm} donates daily-averaged total power of photovoltaic modules per S_w , H_d and H_n donate day period and night period, η_c and η_{dc} donate the efficiencies of charging and discharging of secondary batteries, and P_{tot} donates total power consumption of solar-powered aircraft.

During the nighttime period, there is another balance between the energy stored in secondary batteries and the total power consumption multiplied by night duration.

$$m_{\text{bat}} \kappa_{\text{bat}} \eta_{\text{dc}} = P_{\text{tot}} H_n \quad (3)$$

Here κ_{bat} donates gravimetric energy density of secondary batteries.

Equations (1) to (3) are the basic equations for determining configuration parameters, which distinguish continuous-operation solar-powered airplanes from conventional-powered HALE airplanes. In level flight, the total power consumption contains three parts.

$$P_{\text{tot}} = P_{\text{pld}} + P_{\text{p}} + P_{\text{av}} = P_{\text{pld}} + P_{\text{lev}} / \eta_p + P_{\text{av}} \quad (4)$$

Here P_{pld} , P_{p} , P_{av} and P_{lev} donate the power consumption of payload, propulsion systems, avionics and level flight, respectively. Also, η_p donate the efficiency of propulsion systems.

The first part comes from payload instruments given in the design mission requirements. The second part is for propelling mechanisms to maintain level flight at a certain altitude as shown in Eq. (5).

$$P_{lev} = \frac{m_{tot} g}{(C_L/C_D)} V = W \sqrt{\left(\frac{W}{S_w}\right) \frac{2}{\rho} \frac{C_D}{C_L^{1.5}}} \quad (5)$$

Here V donate flight velocity, C_L and C_D donate coefficients of lift and drag, ρ donate air density, W donate total weight.

The last part is avionics power required for flight control, communication and navigation, etc. It is estimated as a constant fraction of the avionics mass:

$$P_{av} = \zeta_{av} m_{av} \quad (6)$$

Statistically, the power-to-mass ratio of avionics ζ_{av} is estimated about 6.0 W/kg in Ref.[4].

3 Introduction of the Design Methodology

The configuration sizing of solar-powered UAVs differs significantly from traditional HALE airplanes. It can be generalized by two aspects with the energy-centered design guideline[12]. Firstly, all energy in operation only comes from PV modules mounted on the wing or sail tails. Secondly, these surfaces are highly coupled with the aerodynamic characteristics, and their weights of airframe structures and PV modules occupies a large amount of total weight and then influences the total power consumption as shown in Eq. (4) and Eq. (5). Without taking into account geometric sizes of fuselages, horizontal and vertical tails of small wetted areas, there are four characteristic configuration variables for the wing-sail configuration, including wingspan, aspect ratio (AR) of wing (b_w/c_w), chord ratio (c_l/c_w) and area ratio (S_l/S_w) of sail tails to the wing, as shown in Fig. 3. Accordingly, there are two variables of wingspan and AR of wing for the conventional. The platform shapes of the wing and sail tails need to be rectangular with constant chord designs for ease of PV modules integration and ease of manufacture, and all sail tails are considered to be with unified lengths and widths. In Fig. 3, the shadowed parts represent PV modules. The chord ratio (c_l/c_w) is chosen by design experience at the beginning for the wing-sail configuration.

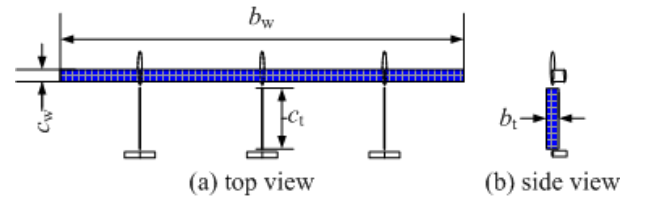


Fig. 3 Top and side views of the wing-sail type and its configuration variables

Fig. 4 is a schematic representation of the flight course for the wing-sail configuration to track the sun's azimuth and elevation angle. The flight course comprises a semicircle end and a straight leg, and both the length of the leg and the diameter of the end are far longer than the wingspan.

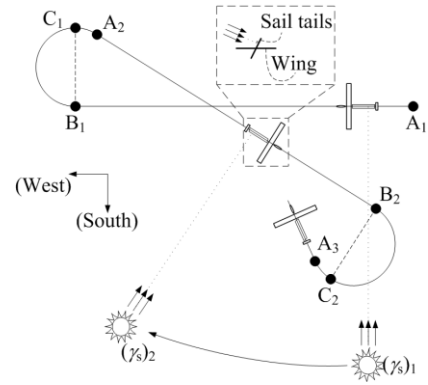


Fig. 4 schematic representation of two adjacent flight courses of Azimuth-Elevation tracking method

In Fig. 4, there are two adjacent flight courses for two adjacent periods. In the first course, it starts from the point A_1 to the point B_1 with the heading direction and corresponding rotating angle of sail tails to maximize solar energy absorption, and then turns right 180 degrees along the semicircle end to the point C_1 . At this moment, the sensor onboard detects the solar azimuth angle and solar elevation angle, and then recalculates the next heading direction. During the period from the point C_1 to the point A_2 , the solar azimuth angle is tracked, named "Azimuth tracking" method. At the same time, sail tails rotate and track the solar elevation angle in the way of "Elevation tracking" method. The second period begins at the point A_2 . In Fig.4, arc B_1C_1 and arc C_1A_2 are concentric, and the length of the legs and the radius of the ends are termed L_{ov} and R_{ov} , respectively. It is not necessary for the conventional configuration with no sail tails to track the Sun, so its flight course is not constrained by the sun's position.

Then, as the theoretical core of this work, the sizing process for the conventional and wing-sail configurations is shown in Fig. 5.

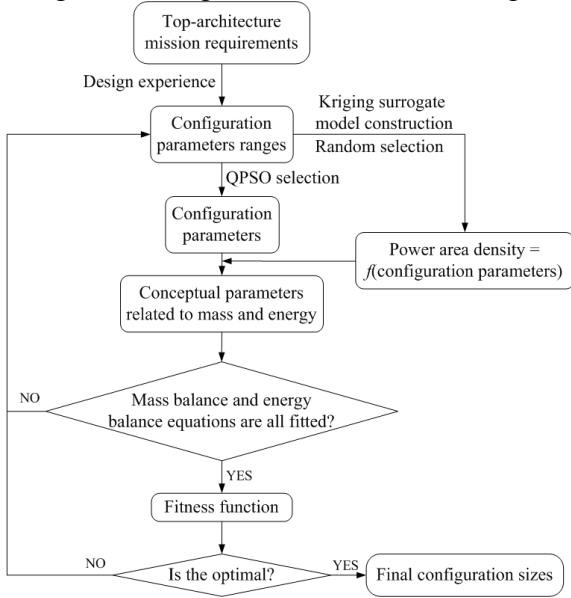


Fig. 5 Sizing process for both configurations

The design process starts from the top-architecture mission requirements, which include operational altitudes, operational latitudes, flight seasons, mass and power of the payload, and tracking method and configuration type. Firstly, the approximate range of each configuration parameter is obtained with design experience. Then, a software package DACE (Design and Analysis of Computer Experiments) in MATLAB® is employed to obtain a Kriging approximation model relating configuration parameters to corresponding power absorption of PV modules in order to save computational costs[16]. With this Kriging approximation model and a group of configuration values randomly selected, conceptual parameters related to the mass and energy are then obtained. If all mass balance and energy balance equations are satisfied, then the fitness value is obtained by the fitness function that links the optimization problem and QPSO algorithm[17]. If the fitness value is optimal, it achieves a group of final configuration sizes. If not, a new group is generated by QPSO algorithm again until the stop criterion is reached. Section IV to section VII will describe the key parts of the configuration design methodology in detail, including power characteristics model of PV modules, mass components parameterization,

aerodynamic efficiency formulation, QPSO algorithm and its fitness function, and Kriging surrogate model.

4 Power Characteristics Model of Photovoltaic Modules

It is well known that PV modules absorb solar radiation effectively if their surfaces point to the direction of solar propagation, while the position of the Sun related to each PV module varies at all times. Here introduces a fixed right-handed gravitational Cartesian coordinate system S , with S_x pointing to the south, S_y pointing to the west, S_z pointing to the nadir, and with the origin in the center of each PV module. The geometric relationships between the beam solar radiation and a plane of any orientation relative to the Earth at any time are described in terms of two angles and two vectors as illustrated in Fig. 6.

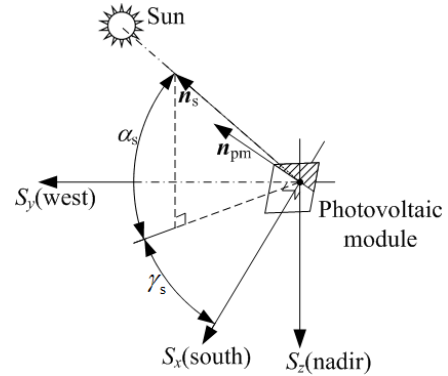


Fig. 6 Position of the Sun relative to an arbitrarily oriented PV module

Only the part of total solar radiation projected on the normal direction of PV modules can be absorbed effectively. The total power from all PV modules of N_{pm} , termed P_{pm} , is defined as:

$$P_{pm} = P_{pm.w} + P_{pm.t} = \sum_i^{N_{pm}} I_{tot} (\eta_{pm} \cos \langle \mathbf{n}_s, \mathbf{n}_{pm} \rangle S_{pm})_i \quad (7)$$

The total power P_{pm} contains two parts: one part from the wing, termed $P_{pm.w}$, and the other part from sail tails, termed $P_{pm.t}$. The total power from all PV modules varies all the time in operation. In a whole day, including the daytime and nighttime, the daily average total power per unit wing area is calculated below:

$$K_{\text{pm}} = \int_{H_d} \frac{P_{\text{pm}}}{S_w (H_d + H_n)} dt \quad (8)$$

4.1 Total Solar Radiation at High Altitude Atmosphere

The radiation spectrum changes in the course of its path through the atmosphere, depending on a number of parameters, such as distance from the Earth to the Sun, altitude, cloud cover, haze content, moisture content, and soil pollution. The total solar radiation contains mainly beam radiation, (also called direct radiation), diffuse radiation and reflected radiation. Due to low-humidity and cloud-free atmosphere in the stratosphere, the reflected radiation component is negligible. Therefore, the total solar radiation is expressed by:

$$I_{\text{tot}} = I_{\text{beam}} + I_{\text{dif}} \quad (9)$$

Here I_{beam} donates beam radiation, and I_{dif} diffuse radiation.

Solar irradiance at mean earth-sun distance, I_{on} , outside the atmosphere is nearly constant, with variation range of $\pm 3.3\%$ in a whole year. The World Radiation Center has adopted a value of $1,367 \text{ W/m}^2$ for the solar constant, termed G_{sc} . The dependence of extraterrestrial radiation on time of year with sufficient accuracy for most engineering calculations is given by[11]:

$$I_{\text{on}} = G_{\text{sc}} \left[1 + 0.033 \cos(360n_d/365) \right] \quad (10)$$

There are several methods for modeling the beam radiation [11, 13, 18], the solar radiation received without scattered by the atmosphere. Taking into consideration the environment in the stratosphere, modeling accuracy, and calculating difficulties, an empirical radiation model is employed in Ref. [13], the radiation attenuation of which is defined as a function of altitude and solar elevation angle:

$$I_{\text{beam}} = I_{\text{on}} \exp \left[- \frac{c_s \exp \left(-\frac{h}{h_s} \right)}{\left[\sin \left(\frac{\alpha_s + \alpha_{\text{dep}}}{1 + \alpha_{\text{dep}}/90} \right) \right]^{s_s + \frac{h}{h_b}}} \right] \quad (11)$$

$$\alpha_{\text{dep}} = 0.57 + \arccos \left[R_E / (R_E + h) \right] \quad (12)$$

Here c_s and s_s are constants, valued 0.357 and 0.678, respectively. h_b and h_s are height constants, valued 40 km and 7 km, respectively. R_E is the Earth radius, valued 6,356.8 km. α_{dep} is depression angle, an altitude correction to solar elevation angle. Equation (11) and (12) for the beam radiation prove sufficiently accurate results in Ref. [13] for the intended application, especially at high altitudes and at shallow angles of incidence. Only at altitudes below about 10 km could significant deviations occur for current weather conditions.

Another radiation component is diffuse radiation, the solar radiation whose direction is scattered by the atmosphere. Under the hypothesis that the diffuse radiation for all directions and radiation angles are considered to be constant, the diffuse radiation, sharing 8% of the beam radiation, is defined by[13]:

$$I_{\text{dif}} = 0.08 I_{\text{beam}} \exp \left(-\frac{h}{h_s} \right) \quad (13)$$

Here h donate flight altitude.

4.2 Orientations of PV Modules and the Line from PV Modules to the Sun

Solar-powered airplanes has variable flight paths in operation, and the position relationships between the Sun and PV modules vary all the time, leading to the fact that the composition of the incident sunlight $\cos(\mathbf{n}_s, \mathbf{n}_{\text{pm}})$ changes at any time. Figure 1 shows that only the solar elevation angle, termed α_s , and the solar azimuth angle, termed γ_s , geometrically determine the unit vector of the direction of radiation propagation, \mathbf{n}_s :

$$\mathbf{n}_s = (\cos \alpha_s \cos \gamma_s, \cos \alpha_s \sin \gamma_s, -\sin \alpha_s)^T \quad (14)$$

The variables α_s and γ_s are expressed and obtained as:

$$\sin \alpha_s = \sin \varphi_{\text{lat}} \sin \delta_s + \cos \varphi_{\text{lat}} \cos \delta_s \cos \theta_h \quad (15)$$

$$\begin{cases} \sin \gamma_s = \frac{\cos \delta_s \sin \theta_h}{\cos \alpha_s} \\ \cos \gamma_s = \frac{\sin \alpha_s \sin \varphi_{\text{lat}} - \sin \delta_s}{\cos \alpha_s \cos \varphi_{\text{lat}}} \end{cases} \quad (16)$$

The terms of the declination, δ_s , and the hour angle, θ_h , above are defined as follows[11]:

$$\delta_s = 23.45 \sin \left(360 \frac{n_d + 284}{365} \right) \quad (17)$$

$$\theta_h = 15(H_s - 12) \quad (18)$$

$$H_s = H_{ct} + \frac{(L_{st} - L_{ct})}{15} + \frac{E_t}{60} \quad (19)$$

$$E_t = 0.0172 + 4.28 \cos B - 7.35 \sin B - 3.35 \cos 2B - 9.732 \sin 2B \quad (20)$$

$$B = \frac{360}{365}(n_d - 1) \quad (21)$$

Here, H_s and H_{ct} are solar time in hours and standard clock time in hours for local time zone, respectively. L_{st} and L_{ct} are standard meridian for the local time zone in degrees and the longitude of the location in degrees, respectively.

Similarly, only attitude angles of the solar-powered UAVs and mounting angles of PV modules determine the normal unit vectors of any PV module, \mathbf{n}_{pm} . The body-axis system, B , is rigidly fixed to the solar-powered UAV, with B_x pointing forward, B_y pointing to the right wing, and B_z being the cross product of B_x and B_y . The attitude angles are based on the body-axis system relative to the frame S , which include yawing, pitching and rolling angles, termed ψ_b , θ_b and ϕ_b , respectively. The mounting angles of PV modules are based on the local coordinate system of each PV module relative to the body-axis system. The local right-handed coordinate system P is rigidly fixed to any PV module, with P_z normal to its plane and P_x paralleling to any boundary. The mounting angles include yaw-deviation, pitch-deviation and rotate-deviation angles, termed ψ_{pm} , θ_{pm} and ϕ_{pm} , respectively. Then, \mathbf{n}_{pm} is derived by transformation:

$$\mathbf{n}_{pm} = \mathbf{L}_{g2b} \mathbf{L}_{b2pm} (0, 0, -1)^T \quad (22)$$

Here \mathbf{L}_{g2b} is the transformation matrix from body-axis coordinate system to fixed gravitational coordinate system, and \mathbf{L}_{b2pm} is the transformation matrix from local coordinate system to body-axis coordinate system.

In level flight, the attitude angles of θ_b and ϕ_b are approximately zero. In addition, the yaw-deviation angle of ψ_{pm} is also approximately zero in order to avoid projected surface area along the freestream. Therefore, the final \mathbf{n}_{pm} is derived from Eq. (22):

$$\mathbf{n}_{pm} = - \begin{pmatrix} \cos \psi_b \sin \theta_{pm} \cos \phi_{pm} + \sin \psi_b \sin \phi_{pm} \\ \sin \psi_b \sin \theta_{pm} \cos \phi_{pm} - \cos \psi_b \sin \phi_{pm} \\ \cos \theta_{pm} \cos \phi_{pm} \end{pmatrix} \quad (22)$$

4.3 PV Modules Temperature Model

Based on the operating principles of solar cells, its absorption efficiency depends on its surface temperature and rarely on total irradiance. Therefore, it is necessary to integrate the thermodynamic model into the design methodology, since the atmosphere in the stratosphere is significantly rare and thin, leaving less air for either conduction or convection to carry the excess heat away. The experimental data in Ref. [19] show that total irradiance received slightly affects the efficiency of Si-cell PV modules in the range from 180 W/m² to 1300 W/m², which is in accordance with the irradiance range in the stratosphere. However, the experimental data for Si-cell PV modules in both Ref. [19] and Ref. [20] show that surface temperature of PV modules from about -80 °C to 50 °C approximately exhibit linear relationship with absorption efficiency. Low temperature leads to high efficiency, while high temperature leads to low efficiency. For other solar cell materials, the temperature characteristics still exist. When the surface temperature of a PV module is T_{sur} , its efficiency is defined by:

$$\eta_{pm} = \eta_{pm0} [1 + C_T (T_{sur} - T_{sur0})] \quad (24)$$

Here, C_T represents the temperature coefficient of a PV module and η_{pm0} represents the standard efficiency of a PV module at the standard surface temperature T_{sur0} , usually 25 °C. Two sides of the wing and sail tails are rigidly connected together through internal supports, such as ribs and beams as illustrated in Fig. 7. Because these connections are of relatively small cross-sectional area, heat transfer through them by conduction is negligible. In addition, both the insides of the wing and sail tails are hollow and closed, filled with only air. As the low conductance through air for internal heat transfer between two sides of the wing and sail tails is also negligible, the control volume for

thermodynamic model is limited for the side exposed to direct sunlight. In Fig. 7, the control volumes are indicated by dashed lines.

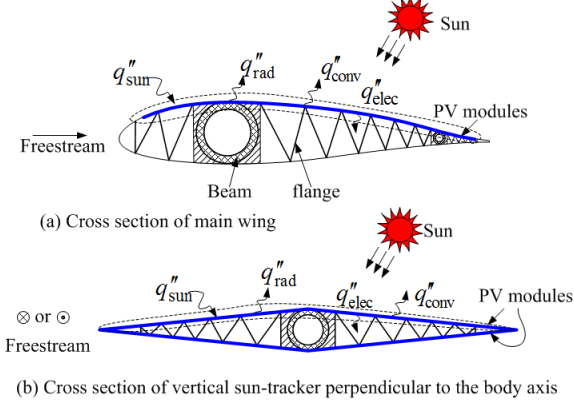


Fig. 7 Control volumes and structures of cross sections for wing and vertical sun-trackers

Therefore, the heat-balance equation could be expressed as[21-23]:

$$\begin{cases} \frac{dT_{\text{sur}}}{dt} = \frac{\dot{E}_{\text{in}} - \dot{E}_{\text{out}}}{m_{\text{pm}}(c_p)_{\text{pm}}} = \frac{q_{\text{sun}}'' - q_{\text{elec}}'' - q_{\text{rad}}'' - q_{\text{conv}}''}{\rho_{\text{pm}}(c_p)_{\text{pm}}} \\ q_{\text{sun}}'' - q_{\text{elec}}'' = (\alpha_{\text{pm}} - \eta_{\text{pm}}) I_s \cos \langle \mathbf{n}_s, \mathbf{n}_{\text{pm}} \rangle \\ q_{\text{rad}}'' + q_{\text{conv}}'' = \varepsilon_{\text{pm}} \sigma (T_{\text{sur}}^4 - T_a^4) + \frac{kNu}{c_{\text{pm}}} (T_{\text{sur}} - T_a) \end{cases} \quad (25)$$

Here, \dot{E}_{in} and \dot{E}_{out} represent the rate of energy transfer entering and leaving any control volume. q'' represents the heat flux. $(c_p)_{\text{pm}}$ represents the specific heat for PV modules. α_{pm} and ε_{pm} represent the absorptivity and emissivity of PV modules, respectively. c_{pm} represents the local chord of the surface with PV modules. k represents the thermal conductivity of atmosphere. T_{sur} and T_a represent the surface temperature of PV modules and atmosphere, respectively. σ represents the Stefan-Boltzmann constant, valued $5.67 \times 10^{-8} \text{ W m}^{-2} \text{ K}^{-4}$.

Convection heat transfer is a mixture of free (or natural) convection and forced convection as expressed in Eq. (27) and Eq. (28), respectively.

$$Nu^{7/2} = Nu_{\text{for}}^{7/2} + Nu_{\text{fre}}^{7/2} \quad (26)$$

$$Nu_{\text{fre}} = \left\{ 0.825 + \frac{0.387Ra^{1/6}}{\left[1 + (0.492/Pr)^{9/16} \right]^{8/27}} \right\}^2 \quad (27)$$

$$\begin{cases} Nu_{\text{for}} = Pr^{1/3} \left[0.037 \left(Re_x^4 - Re_x^4 \right) + 0.664 Re_x^{1/2} \right] \\ Re_x = r_{\text{lam}} Re \end{cases} \quad (28)$$

$$\begin{cases} Ra = \frac{g \rho^2 (T_{\text{sur}} - T_a) c_{\text{pm}}^3}{T_a \mu^2} \\ Re = \frac{c_{\text{pm}}}{\mu} \sqrt{\frac{2\rho W}{C_L S_w}} \\ Pr = \frac{(c_p)_a \mu}{k} \end{cases} \quad (29)$$

Here Ra , Re , Nu and Pr denote Rayleigh number, Reynolds number, Nusselt number and Prandtl number respectively. μ denotes the dynamic viscosity of the atmosphere. $(c_p)_a$ denotes specific heat for the atmosphere, valued $1,004 \text{ J kg}^{-1} \text{ K}^{-1}$. r_{lam} denotes the ratio of laminar flow and Re_x denotes local Reynolds number at the transition point. Equations (26) to (28) for heat transfer analysis are limited under the conditions of incompressible flow, $0.6 \leq Pr \leq 60$, and $Re_x \leq Re \leq 10^8$ [21].

5 Mass Components Parameterization

As listed in Eq. (1), the total mass is divided into eight parts. In this section, it will go through all the parts and establish their mass models respectively. The payload mass is given in the design requirements, not dependent upon the configuration parameters.

5.1 Airframe Structure

Usually, the statistical weights methods are used in conceptual design. However, with a small number of solar-powered airplanes in the history[8], researchers mostly used sailplanes' structure mass estimation instead [4, 8]. For large-wingspan and high aspect-ratio wing, the structure mass estimated by those models results in high wing loading, leading to no feasibility of continuous flight in the stratosphere[12]. From the Pathfinder up to the Helios prototype, the structure mass per unit wing area has been kept under control through the span-loader guideline[10, 24]. It means that total mass is

distributed along the wingspan, and it is likely that the whole airplane is connected wingtip-to-wingtip together by a series of small airplanes. Therefore, the airframe structure mass per unit wing area has little relevance to the wingspan and AR of wing. Then, the structure mass is proportional to the area:

$$m_{af} = (1 + r_{af.w}) \rho_{af.w} S_w + \rho_{af.t} S_t \quad (30)$$

$$= \left[(1 + r_{af.w}) \rho_{af.w} + r_s \rho_{af.t} \right] S_w$$

The $r_{af.w}$ term represents the weight ratio of fuselages, horizontal tails, and nacelles for propulsion systems to the wing. The $\rho_{af.w}$ term and $\rho_{af.t}$ term respectively represent surface densities of airframe structure for the wing and sail tails. Statistically, the total structure mass per unit wing area of several HALE solar-powered airplanes is estimated: Pathfinder's 1.95 kg/m²[25], Zephyr's 1.1 kg/m², HeliPlat's 2.0 kg/m²[6], and Solar Impulse's 3.5 kg/m² [26].

5.2 PV Modules

The solar cells are interconnected electrically and then encapsulated between two non-reflective transparent layers to obtain a PV module. Therefore, the surface density of PV modules includes both solar cells and the encapsulation. The surface density of PV modules on the wing, termed $\rho_{pm.w}$, is relatively higher than that on sail tails, termed $\rho_{pm.t}$, in that the flexibility and aerodynamic loads of the former are higher than those are on the latter. The PV modules mass can be estimated by:

$$m_{pm} = S_{pm.w} \rho_{pm.w} + 2S_{pm.t} \rho_{pm.t} \quad (31)$$

$$= \left(\xi_{pm2w} \rho_{pm.w} + 2r_s \xi_{pm2t} \rho_{pm.t} \right) S_w$$

Here $S_{pm.w}$ and $S_{pm.t}$ represent total areas of PV modules on the wing and sail tails respectively, and $\rho_{pm.w}$ and $\rho_{pm.t}$ represent surface densities of PV modules on the wing and sail tails respectively. ξ_{pm2w} and ξ_{pm2t} represent area ratios of PV modules to their mounted wing and sail tails, respectively, which are both lower than 1.0.

5.3 Maximum Power Point Tracker

Generally, the MPPT mass is proportional to the peak power of all PV modules throughout

the operation with an approximate constant power-to-mass ratio, termed ζ_{mppt} . The MPPT mass can be defined by:

$$m_{mppt} = \left(P_{pm} \right)_{\max} / \zeta_{mppt} \quad (32)$$

5.4 Secondary Batteries

Concerning the battery, its mass is directly proportional to the energy storage needed in the nighttime, which is proportional to total power consumption and night duration, and inversely proportional to its gravimetric energy density and discharging efficiency.

$$m_{bat} = \frac{H_n P_{tot}}{\kappa_{bat} \eta_{dc}} \quad (33)$$

5.5 Propulsion Systems

A propulsion system usually contain three subparts (motor and its control electronics, propeller), usually not including gearbox owing to the reliability in long-endurance operation and the extreme environment in the stratosphere. As a whole, the propulsion systems mass is proportional to the maximum continuous shaft power, termed $(P_p)_{\max}$, and inversely proportional to the power-to-mass ratio, termed ζ_p . Although the main flight condition is in the quiescence flight, higher power should be considered for taking-off, climbing, and flying against prevailing wind in the stratosphere and turbulence in low altitudes. Generally, the ratio of maximum continuous shaft power to shaft power in level flight, termed ξ_p , is about 2 to 3. The propulsion systems mass is defined by:

$$m_p = \frac{(P_p)_{\max}}{\zeta_p} = \frac{\xi_p P_{lev}}{\eta_p \zeta_p} \quad (34)$$

5.6 Avionics and Landing Gear

The contributions of avionics and landing gear to the total mass buildup are of relatively small magnitude, but should be included for completeness. Avionics and landing gear are estimated as constant fractions of gross mass:

$$m_{av} + m_{lg} = r_{av} m_{tot} + r_{lg} m_{tot} \quad (35)$$

Statistically, the avionics weight fraction, termed r_{av} , is estimated about 0.03 in Ref.[4] ,

and the landing gear weight fraction, termed r_{lg} , is estimated about 0.00725 in Ref.[18].

6 Aerodynamic Efficiency Formulation

The $C_D/C_L^{1.5}$ term in Eq. (5) is named as endurance parameter for solar-powered UAVs, whose terms C_D and C_L are correlated in Ref.[27] by:

$$C_D = C_{D0} + \frac{C_L^2}{\pi A_w e} \quad (36)$$

Here C_{D0} donate the coefficient of parasite drag.

The Oswald efficiency factor e in Eq. (36) varies with wing aspect ratio. Solar-powered UAVs usually use rectangular wing with the same cross sections and with little twist in order to maximize PV modules and reduce manufacturing costs. To obtain the actual e for rectangular wing of high aspect ratio, a series of wings with aspect ratios from 10 to 60 are calculated with classic lifting-line theory using nonlinear section lift data[28]. The airfoils used are E387 and FX 63-137, representative of low Reynolds airfoils. The section lift data are obtained by XFOIL[29] in the conditions of Mach number of 0.15, and Reynolds number of 500,000, as shown in Fig. 8. The first-order exponential decay fit of all the calculation result for e is:

$$e = 0.303 \exp(-A_w/30.9) + 0.695 \quad (37)$$

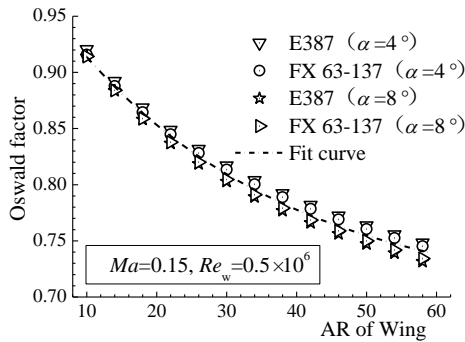


Fig. 8 Tendency of Oswald factor for rectangular wings with aspect ratios from 10 to 60

Then, the Component Buildup Method[27] is used to calculate the parasite-drag coefficient C_{D0} in Eq. (36), which is mainly built up by the wing and sail tails. The parasite drag from fuselages, distributed propulsion nacelles and other miscellaneous components are considered by a scaling factor, termed r_f , in Eq. (38):

$$C_{D0} = r_f r_{LP} \frac{2S_w C_{f,w} FF_w + 2S_t C_{f,t} FF_t}{S_w} = \quad (40)$$

$$C_{f,w} = \frac{1.328}{\sqrt{Re_w}} r_{lam,w} + \frac{0.455}{(\log_{10} Re_w)^{2.58}} (1 - r_{lam,w}) \quad (41)$$

$$C_{f,t} = \frac{1.328}{\sqrt{Re_t}} r_{lam,t} + \frac{0.455}{(\log_{10} Re_t)^{2.58}} (1 - r_{lam,t}) \quad (42)$$

$$Re_t = r_c Re_w \quad (43)$$

For the wing-sail configuration, the component form factors of the wing and sail tails, termed FF_w and FF_t , are equal to 1.25 and 1.1 empirically, respectively. The chord ratios of laminar flow of the wing and sail tails, termed $r_{lam,w}$ and $r_{lam,t}$, are equal to 0.2 and 0.0 empirically, respectively. The scaling factor r_f is equal to 1.25 based on the wetted area ratios of fuselages and nacelles to reference wing area. r_{LP} donates the interference drag by distributed propellers, valued 1.07 in Ref.[6].

There are two efficient conditions for level flight from flight mechanics theory: the minimum thrust required and the minimum power required. In real flight, the minimum power required is preferred for solar-powered airplanes. However, the minimum thrust required is considered in the design methodology. In this flight condition, the lift coefficient C_L is defined as:

$$C_L = \min(\sqrt{\pi A_w e C_{D0}}, (C_L)_{up}) \quad (42)$$

Here $(C_L)_{up}$ is the upper limit of the cruise lift coefficient, valued by 1.25 with design experience.

7 Optimization Formulations

It is obvious that configuration sizes and other conceptual parameters are nonlinearly coupled by energy. Besides, under the constraints of both energy balance and mass balance, the solution space for configuration sizes is wide. Therefore, it is necessary to employ multi-objective optimization method to achieve the optimal matching of conceptual parameters. Here, QPSO algorithm and Kriging surrogate model are employed.

7.1 QPSO algorithm

Particle Swarm Optimization, first introduced by Kennedy and Eberhart[30] in 1995, is a population based optimization technique inspired by social behavior of bird flocking or fish schooling. Due to the fact that the PSO algorithm is simpler and more feasible than other non-gradient based algorithms, it is widely applied in the areas of airfoil[31] and wing [32] optimization and preliminary aircraft configuration optimization[33]. However, in this algorithm, each particle moves along a determined trajectory in Newtonian mechanics, lacking global-convergence guarantee. Then, Sun[17, 34] presented an improved PSO algorithm in 2004, called Quantum-Behaved Particle Swarm Optimization (QPSO). Its individual particle can appear in any position of the whole solution space, and QPSO have more excellent global searching ability. The formulations of QPSO algorithm are given by[17]:

$$X_i^{j+1} = \left[(X_i^p)^j u_1 + (X^g)^j (1-u_1) \right] \pm \beta \left| (mbest)^j - X_i^j \right| \ln \left(\frac{1}{u_2} \right) \quad (43)$$

$$(mbest)^j = \frac{1}{M} \sum_{i=1}^M (X_i^p)^j \quad (44)$$

Here, each particle, X , in QPSO algorithm has two variables of configuration parameters, including wing AR, the area ratio of sail tails to the wing. In Eq. (43) and Eq. (44), X_i^j is the position of particle i at generation j . X_i^p is the best position found by particle i so far, and X^g is the best position among all the particles in the population.

The design ranges for two variables are determined experientially before optimal design. The process can be outlined as follows:

- (1). Create an initial randomly distributed swarm of M particles with initial position information restricted by an appropriate Euclidean distance, and each particle must fit basic equations of energy balance and mass balance.
- (2). Calculate the Mean Best Position $mbest$ among the particles by Eq. (44).

- (3). Evaluate the desired fitness function for each particle and compare with the particle's previous best values, and then set the best value to the current value if the current value is better.
- (4). Determine the current global best position among the particle's best positions. Compare the current global position to the previous, and then set the global position to the current global if the current global position is better.
- (5). Generate M new particles by Eq. (43) restricted by the Euclidean distance, and each new particle must fit basic equations.
- (6). Repeat steps (2)-(5) until a stop criterion is satisfied OR a pre-specified number of generations are completed.

If a QPSO particle fit basic equations, it can obtain a group of conceptual parameters. Three conceptual parameters of payload weight fraction, wing AR and cruise velocity are chosen for fitness calculation of each particle. Higher payload weight fraction means better payload-carrying ability and lower costs, lower AR of wing A_w means less flexible, and larger cruise velocity V has more advantages to go against prevailing winds. The fitness function employs a multi-objective nonlinear weighting method, which is expressed by:

$$\begin{cases} F_{\text{fit}} = \sum_i A_i \cdot 2^{f(v_i)} \\ f(v_i) = \begin{cases} \exp(v_i) & v_i \leq 1 \\ \exp(1) \cdot v_i & v_i > 1 \end{cases} \\ v_i = 1 - 2 \frac{(C_{\text{new}})_i - (C_{\text{bad}})_i}{(C_{\text{good}})_i - (C_{\text{bad}})_i} \end{cases} \quad (45)$$

The term C_{new} corresponds to the present values of evaluation parameters, the term C_{bad} corresponds to the given unacceptable values, and the term C_{good} corresponds to the given satisfying values. If the i_{th} evaluation parameter $(C_{\text{new}})_i$ is near its $(C_{\text{bad}})_i$, the intermediate variable v_i is large, leading to the fact that its contribution to F_{fit} is also large. If the i_{th} evaluation parameter $(C_{\text{new}})_i$ is near its $(C_{\text{good}})_i$, it contributes little to F_{fit} . Therefore, the less the term F_{fit} is, the better the group of configuration values is.

7.2 Kriging surrogate model

When solving the basic equations for each group of configuration parameters in each QPSO particle, it has to recalculate the daily averaged total power per unit wing area and the maximum total power of PV modules by minor time step. It leads to expensive calculations. Therefore, the Kriging approximation model is utilized as a surrogate to estimate power characteristics of PV modules quickly and precisely. As depicted in the flow chart of Fig. 9, the processes of Kriging surrogate model construction is based on the data from the computer experiment.

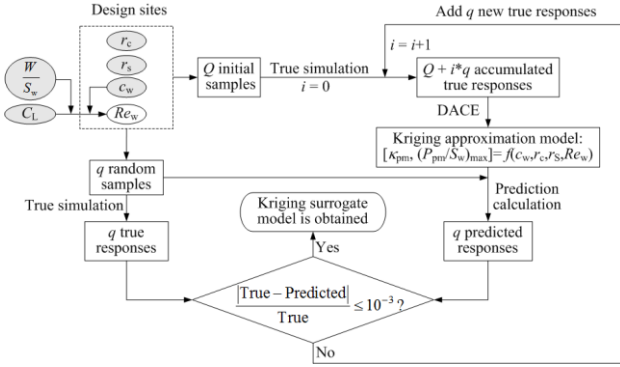


Fig. 9 Flow chart for building Kriging Surrogate model

The input samples contain four parameters in design sites: r_c , r_s , c_w and Re_w . The ranges of the first three parameters are given experientially. The range of Re_w is derived from its definition expression in Eq. (46), and the ranges of lift coefficient and wing loading in Eq. (46) are given statistically.

$$Re_w = \frac{\rho c_w V}{\mu} = \frac{c_w}{\mu} \sqrt{\frac{2\rho}{C_L}} \sqrt{\frac{W}{S_w}} \quad (46)$$

True responses can be obtained from input samples by true simulation, and the input samples and true responses are used for constructing the Kriging approximation model with the software package DACE. Then, predicted responses can be obtained from any input sample by this approximation model as a surrogate. If the differences between predicted responses and true responses are within the given criterion, the construction procure is over. If not, it is necessary to add more input samples and true responses. In this paper, the number of initial samples, termed Q , is 20. The number of

newly added samples, termed q , is 20, and the number of iterations is about 3 to 5. That is, the total number of whole samples ranges from 80 to 100. As the particles generated in QPSO, the samples are also randomly distributed in the design sites by an appropriate Euclidean distance.

8 Application of the Design Methodology

Until now, the design methodology for year-round solar-powered stratospheric UAVs has been established. The following researches are focused on its applications for both configurations, especially the wing-sail type.

8.1 Mission Requirements and Input Parameters

There are about forty parameters contained in the formulations of the methodology. It is necessary to distinguish among four different groups.

The first group is composed of configuration variables, including AR of wing, wing chord, chord ratio and area ratio of sail tails to the wing. At the beginning, the design space for each configuration size is generally given by experience: A_w on [20, 60], c_w on [2 m, 6 m] and r_s on [0, 1]. The chord ratio of sail tails to the wing, r_c , is valued 5.0 by design experience. In addition, wing loading and lift coefficient statistically ranges from 20 N/m² to 80 N/m² and 0.6 to 1.4, respectively. Then, Re_w ranges from 0.22×10^6 to 2.1×10^6 by Eq. (46) for Kriging surrogate model construction.

The second group is composed of parameters linked to the design mission, which are operational altitude, seasons, operational latitude, mass and power consumption of the payload, and the configuration type. A top-architecture design mission in the stratosphere for year-round operation is given as follows.

- Operational altitude: 20 km
- Operational longitude: 120 °N
- Flight duration: > one year (continuous operation)
- Payload weight: 300 kg
- Payload power: >3000 W

- Operational latitude and Configuration: defined in the following

The third group comprises of parameters that are linked to the technology levels and are constant or can be considered as constants. A list of these parameters is presented in Table 1. The parameters related to PV modules are from silicon solar cells in Ref.[22] , which are practically mature and used by most solar-powered airplanes. The parameters for secondary batteries are from Lithium-Sulfur (Li-S) Batteries of high specific energy and maturity.

Table 1 Input constants for each component

Parameter	Value	Parameter	Value
$\rho_{af.w}$	1.1 kg m ⁻²	η_p	0.72
$\rho_{af.t}$	0.5 kg m ⁻²	η_{pm0}	0.21
$\rho_{pm.w}$	0.6 kg m ⁻²	ξ_{pm2w}	0.85
$\rho_{pm.t}$	0.45 kg m ⁻²	ξ_{pm2t}	0.95
ζ_{mppt}	2200 W kg ⁻¹	C_T	-0.0045 K ⁻¹
ζ_p	400 W kg ⁻¹	$(c_p)_{pm}$	712 J K kg ⁻¹
ζ_{av}	6 W kg ⁻¹	α_{pm}	0.8
ξ_p	2.5	ε_{pm}	0.85
r_{lg}	0.00725	κ_{bat}	600 W h kg ⁻¹
r_{av}	0.03	η_c	0.95
$r_{af.w}$	0.15	η_{dc}	0.95
r_f	1.25	r_{LP}	1.07

Table 2 Parameters for fitness function

Evaluation parameters	$(C_{good})_i$	$(C_{bad})_i$	Δ_i
r_{pld}	0.18	0.12	1
V	1.1×V _w	0.9×V _w	0.25
A_w	25	45	0.2

The last group comprises of parameters from the Kriging surrogate model, the QPSO algorithm and its fitness function. As to the Kriging surrogate model construction, the Euclidean distance is 0.5, the number of initial samples and newly added samples of every iteration step are 20 and 20 respectively, and the number of iterations to achieve the stop criteria of 1×10⁻³ in Fig. 9 is usually 3~5. As to the QPSO algorithm, the Euclidean distance is equal to 0.4, a swarm size of 80 particles is used, the total number of generations is 40, and the Contraction-Expansion Coefficient β linearly decrease from 1.0 to 0.5 with the generation

increasing. The evaluation parameters of the fitness function are summarized in Table 2.

In Table 2, V_w donates the chosen wind velocity. Usually, solar-powered stratospheric UAVs should be able to against 90-percentile or 95-percentile winds. Based on year-round wind data at the altitudes of 18 km to 20 km in Ref.[4] , the wind velocity of 35 m/s is chosen to constraint the design speed.

8.2 Comparative Analysis on Conceptual Parameters of Both Configurations

Firstly, daily averaged power area densities of PV modules mounted on the wing and sail tails as a function of operational latitudes at the altitude of 20 km are compared as shown in Fig. 10. κ_{pmh} refers to the wing and κ_{pmt} refers to tracking sail tails. Four typical days are chosen, including the sprint equinox, the summer solstice, the autumn equinox and the winter solstice.

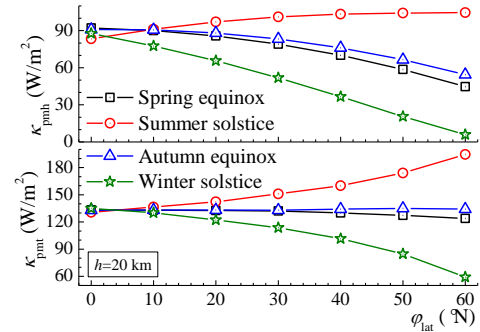


Fig. 10 Comparisons between κ_{pmh} and κ_{pmt} at 20 km

From the equator to 60 °N, the changing tendencies of both κ_{pmh} and κ_{pmt} with the increasing of operational latitudes are the same. Higher latitudes near the winter seasons lead to smaller values, while higher latitudes near the summer seasons lead to larger values. At low latitudes, the variations in both κ_{pmh} and κ_{pmt} throughout a whole year are of slight degree, and κ_{pmt} of sail tails is generally higher than κ_{pmh} of the wing by 52~93 percent. However, at middle latitudes, their variations throughout a whole year show significant and κ_{pmt} of sail tails is higher than κ_{pmh} of the wing by 93~898 percent in that κ_{pmh} is closer to zero near the winter seasons if the operational latitude is closer to the Arctic Circle of 66.5 °N.

Then, with input parameters and mission requirements in the section A, optimized conceptual parameters for both configurations from the latitudes of the Equator to 50 °N are compared in Fig. 11. Two days of the summer solstice ($n_d=173$) and the winter solstice ($n_d=356$) are chosen. In Fig. 11, the researched parameters contain the configuration sizes (b_w and A_w), power absorption (K_{pm}), aerodynamic efficiency (C_L and C_L/C_D) and payload-carrying capacity (r_{pld}).

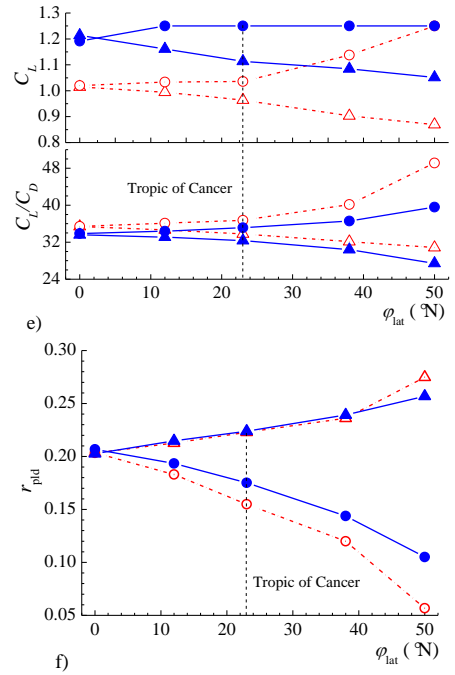
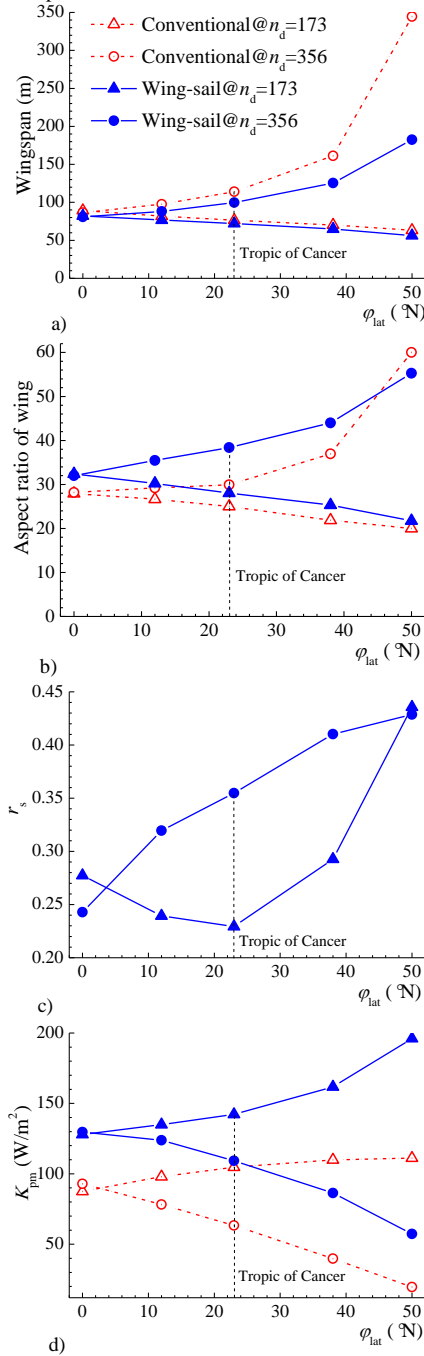


Fig. 11 Comparisons of conceptual parameters for both configurations

As to the conventional configuration depicted by dash-dot lines with hollow triangles and circles, from low to middle latitudes, b_w and A_w decrease during summer and increase during winter, K_{pm} increase during summer and decrease during winter, C_L and C_L/C_D decreases during summer and increase during winter, and r_{pld} increases during summer and decrease during winter. With the energy-centered guideline, K_{pm} acts as the key influential factor. Higher K_{pm} leads to smaller total areas of PV modules required and then saves the weights of structure, PV modules and secondary batteries, and finally leads to higher r_{pld} because of the smaller total weight. Meanwhile, b_w decreases because of the smaller wing area required. In addition, higher K_{pm} also leads to less demand for aerodynamic efficiency of C_L and C_L/C_D and then lower A_w by the fitness function. On the contrary, lower K_{pm} leads to larger total areas of PV modules required and then increases the weights of structure, PV modules and secondary batteries, and finally leads to lower r_{pld} because of the larger total weight. In addition, lower K_{pm} leads to more demand for higher aerodynamic efficiency of C_L and C_L/C_D and then higher A_w .

As to the wing-sail configuration depicted by solid line with solid triangles and circles, the

changing tendencies of b_w , A_w , C_L , C_L/C_D and r_{pld} from low to middle altitudes are the same as the conventional for the similar reasons. In addition, r_s increases continuously during winter with increasing latitudes, but decreases from the equator to the Tropic of Cancer and then increases subsequently during summer. It is because that the improved amplitude of κ_{pmt} compared to κ_{pmh} as depicted in Fig. 10 is the lowest on the summer solstice on the Tropic of Cancer and increases from low to middle altitudes on the winter solstice. Comparatively speaking, the installation of sail tails increase the parasite drag coefficient C_{D0} , so higher A_w for the wing-sail at the same latitude is employed leading to larger C_L to cover the loss of C_L/C_D .

Comprehensively speaking, at low latitudes, the conventional and the wing-sail are both suitable for year-round operation and the latter does not show much superiority over the former. At middle latitudes, two typical design points of the summer solstice and the winter solstice differ greatly for both configurations. However, the employment of the tracking sails by the wing-sail can bridge the gap to some degree, and shorten the wingspan, reduce the total area of PV modules and the overall weight. Thus, it is obvious that the wing-sail outperforms the conventional for year-round operation at middle latitudes. The higher the latitude, the more remarkable the superiority is.

8.2 Application of Design Methodology on the Wing-Sail Configuration at Middle Latitudes

The design methodology developed from section III to section VII could be equally applied to the conventional and the wing-sail configurations. In view of limited researches to explore the year-round operational potentials at middle latitudes by solar power, following sections are focused on the application of design methodology on the wing-sail configuration. The following proposed concept is named "PoXiao" which means breaking dawn after flight throughout the whole night. The latitude of 45° N within middle latitudes and the winter solstice poorest in solar radiation at middle latitudes are chosen for design requirements of

the operational latitude and flight duration. With other input parameters in section A, the optimized design specifications of PoXiao are listed in Table 3.

Table 3 Optimized design specifications

Parameter	Value	Parameter	Value
b_w	152.3 m	m_{af}	689.0 kg
c_w	3.06 m	m_{pm}	322.2 kg
A_w	49.8	m_{bat}	783.3 kg
S_w	466.0 m ²	m_{mppt}	51.3 kg
r_s	0.42	m_p	168.6 kg
S_{pm}	582.0 m ²	m_{lg}	17.6 kg
C_L	1.25	m_{av}	72.7 kg
C_L/C_D	38.1	m_{pld}	300 kg
Re_w	0.58×10^6	m_{tot}	2404.7 kg
V	29.9 m s ⁻¹	W/S_w	50.62 N m ⁻²
K_{pm}	63.4 W m ⁻²	r_{pld}	0.125

As mentioned during the weight estimation for airframe structure, a lower structural weight for a platform with high aspect ratio wing can be obtained by the span-loader guideline. It is likely that a series of modular units is fixed together in a wingtip-to-wingtip manner, forming a single flying surface of great size. The planforms of PoXiao is illustrated in Fig. 12. Only one side of each sail tail is placed with PV modules. In the Fig. 12 c), the terms $\varphi_{pm,t}$ and $\varphi_{pm,h}$ donate the rotation-deviation angles of PV modules on sail tails and the wing with dihedral angles. When the local dihedral angle is positive, $\varphi_{pm,h}$ is positive on the left wing and negative on the right wing.

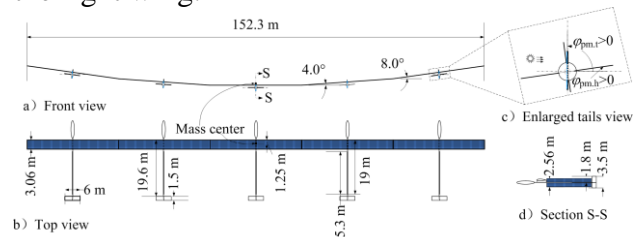


Fig. 12 Configuration sizes of PoXiao concept

From the point of view of geometry sizes, PoXiao is divided into five equal units. The volume coefficients of horizontal tails and vertical tails are 0.6062 and 0.00711, respectively. The three-dimensional view of PoXiao concept and the enlarged view of its single unit are illustrated in Fig. 13.

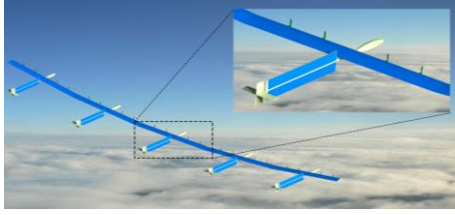


Fig. 13 PoXiao optimized configuration

In the following, the energy performance and characteristics of stability and control of wing-sail PoXiao concept are investigated, respectively.

8.4 Analysis on Energy Characteristics of PoXiao Concept

The winter solstice and the summer solstice are selected for the energy simulations that start at sunrise and last 40 hours as depicted in Fig. 14. PoXiao takes off at the sea level with 60% of batteries capacity, and climbs to the operational altitude of 20 km with the maximum continuous shaft power of 67.5 kW. During taking off and climbing, the overall efficiency of the propelling system is assumed constant. The length of straight leg L_{OV} is 40 km, and the radius of the semicircle end R_{OV} is 2 km.

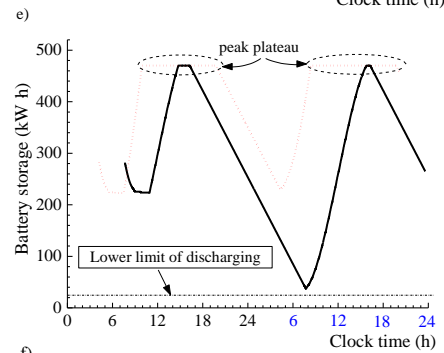
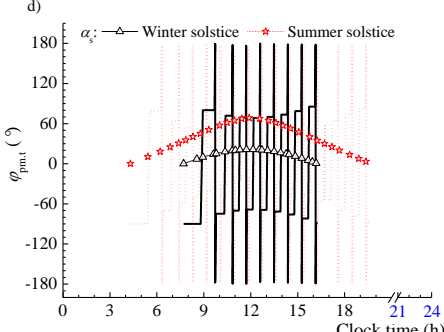
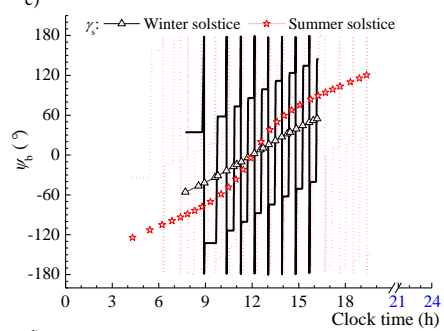
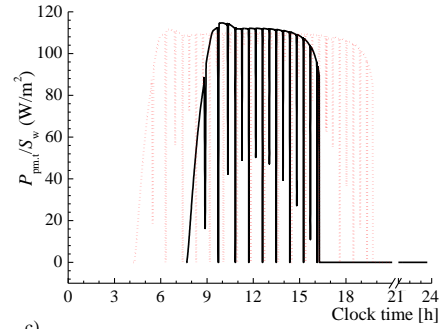
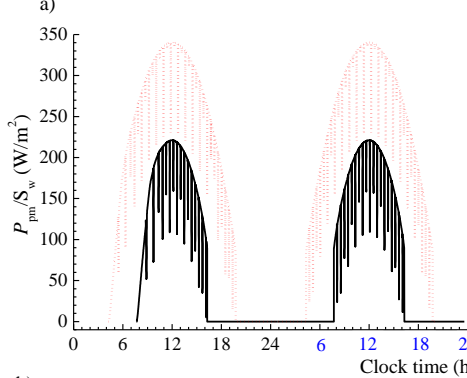
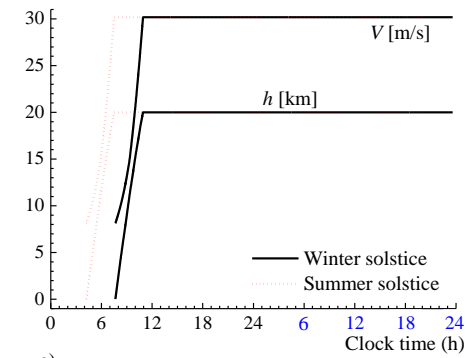


Fig. 14 Continuous flight simulation of PoXiao concept

Figure 14 contains six parts. The first part, Fig. 14 a), includes the performances of flight altitude and flight velocity. The climb phases last about 3.2 hours on both days, and the climb rate is less than 2 m/s. The second and the third parts respectively show power absorption of PV modules per unit wing area for PoXiao concept and for its tracking sails, respectively. For clarity, the period from 21 o'clock on the first day to 21 o'clock on the second day is hidden in Fig. 14 c) to e) because of repetition. PV

modules on the tracking sails oriented normal to the sun's elevation angle can collect a maximum of solar energy in the daytime as compared to PV modules horizontally disposed, i.e. those mounted on wing upper surfaces. Tracking sails contribute significantly to total power absorption, especially at dawn when PoXiao has exhausted most of stored energy in secondary batteries. The fourth part, Fig. 14 d), includes solar azimuth angle, γ_s , and flight-heading direction of PoXiao, ψ_b . The fifth part, Fig. 14 e), includes solar elevation angle, α_s , and rotate-deviation angle of sail tails, $\varphi_{pm,t}$, for tracking the Sun. On the purpose of maximizing power collection, the heading direction is perpendicular to the direction of solar propagation, i.e., $\gamma_s = \psi_b \pm 90^\circ$ or $\gamma_s = \psi_b \pm 270^\circ$, the rotate-deviation angle of sail tails is adapted related to the heading direction, i.e., $\varphi_{pm,t} = -90^\circ + \alpha_s$ or $\varphi_{pm,t} = 90^\circ - \alpha_s$. The adaptation of rotate-deviation angle is finished during the turnaround of the prescribed course. The final part, Fig. 14 f), displays the cycles of discharging and charging of secondary batteries. The peak plateaus mean that the battery is fully charged, while the lowest points mean the battery capacity margins. For the critical design condition of the winter solstice, PV modules can collect enough solar energy for mission flight and fully charging secondary batteries in the daytime, and the stored energy in secondary batteries can fit mission flight in the nighttime. It validates the proposed design methodology. In Fig. 14 f), wide peak plateaus indicate that the power absorption is surplus, which usually occurs near summer. In addition, large battery capacity margin allows the platform to either increase operational altitude or increase the electrical load of mission payload. Experientially, higher payload power and higher altitude means larger covered area of interest and higher mission effectiveness for solar-powered platforms.

Further, the mission capabilities of operational altitude and payload power at middle latitudes throughout a whole year are explored respectively, as illustrated in Fig. 15. The selected latitudes are 30 °N, 45 °N and 55 °N. The lift coefficient is 1.25 and the lift-to-

drag ratios at different altitudes are calculated with Eq. (38) ~ Eq. (41) according to Reynolds number. The efficiency of the propulsion system at different altitudes is assumed constant. In Fig. 15 a), the payload power is a constant of 3 kW, and continuous-operation simulations are carried out to obtain the achievable station-keeping altitudes at different middle latitudes. In Fig. 15 b), the operational altitude is fixed at 20 km, and continuous-operation simulations are carried out to obtain maximum continuous power consumption of payload at different middle latitudes.

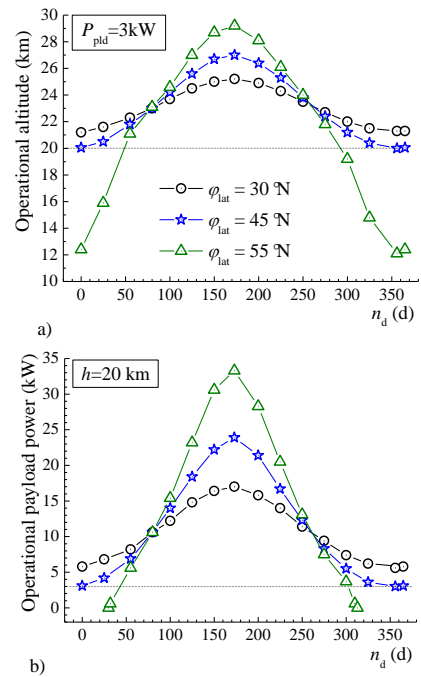


Fig. 15 Mission capabilities at middle latitudes

In general, mission capabilities in Fig. 15 are highly dependent on solar flux distributions in different latitudes. As to altitude capability, operational altitudes in or near summer are higher than those in or near winter are. From 30 °N to 45 °N and to 55 °N, the differences of operational altitude between the summer solstice and the winter solstice change from 4 km to 7 km and to 17 km. As to payload power capability, payload instruments are allowed to consume much more power in or near summer than in or near winter. At the latitude of 55 °N, the payload power reaches 10 times that of design value in summer. However, PoXiao cannot maintain station keeping at 20 km though the payload power is zero during the periods from $n_d=0$ to $n_d=31$ and from $n_d=311$ to

$n_d = 365$, and it is necessary to decrease the operational altitude.

8.4 Preliminary analysis on Stability and Control of PoXiao Concept

Stability and control derivatives in longitudinal and lateral directions are estimated by an extended vortex-lattice model modified based on Athena Vortex Lattice (AVL) code from MIT. The wing incidence is 4 deg, and the horizontal tails incidences are 1 deg. The wing employs an optimized low Reynolds airfoil based on FX 63-137, and the airfoils of horizontal, vertical and sail tails are all treated as flat plates. The lifting surfaces are represented as single-layer vortex sheets discretized into horseshoe vortex filaments, and fuselages like prolate spheroids are modeled via source-doublet filaments. The number of horseshoe vortices is 18×94 for the wing, is 12×12 for each horizontal tail, is 12×12 for each vertical tail, and is 25×10 for each sail tail. The total number of horseshoe vortices is 4382. The modeling fuselages do not extend backwards and pass through sail tails. The 3D model of the vortex lattice method is illustrated in Fig. 15, the rotate-deviation angle of which is -45° . The reference point in the input file is located at the center of gravity that does not change during rotation of sail tails. The hinges of each elevator is located at 60% of local chords and that of each rudder is located at 40%.

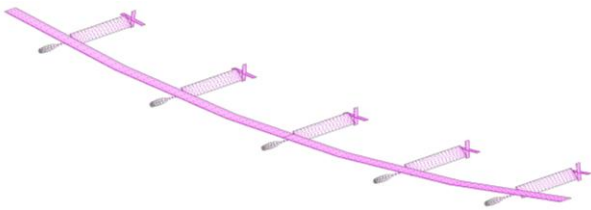


Fig. 15 3D model for vortex-lattice method($\varphi_{pm,t} = -45^\circ$)

Aerodynamic parameters in equilibrium for the conventional configuration with no sails and the wing-sail configuration with the rotate-deviation angles equal to -90° , -45° , and 0° are displayed in Table 3, which include stability and control derivatives, static margins, elevator and rudder deflections for trim, and Oswald efficiency factors. Aerodynamic parameters for $\varphi_{pm,t} = 90^\circ$ are the same as those for $\varphi_{pm,t} = -90^\circ$. Aerodynamic parameters of $C_{n\alpha}$, C_{nq} , $C_{m\beta}$ for

$\varphi_{pm,t} = 45^\circ$ are opposite to those for $\varphi_{pm,t} = -45^\circ$, while the other parameters are approximately the same. Assuming that propulsion systems do not generate unbalanced moments on the aircraft, each elevator deflects the same angle to trim the pitching moment and each rudder deflects the same angle to trim the yawing moment.

Table 4 Aerodynamic parameters in equilibrium

Parameter	No sails	-90°	-45°	0°
e	0.798	0.797	0.794	0.798
$C_{L\alpha}$ (rad^{-1})	6.13	6.13	6.19	6.25
$C_{m\alpha}$ (rad^{-1})	-0.96	-0.96	-1.04	-1.12
SM (%)	15.73	15.73	16.77	18.00
$C_{n\alpha}$ (rad^{-1})	0	0	1.7E-3	0
C_{mq} (rad^{-1})	-20.65	-20.65	-22.58	-24.71
C_{nq} (rad^{-1})	0	0	0.041	0
$C_{m\delta e}$ (rad^{-1})	-1.220	-1.220	-1.243	-1.278
$C_{m\beta}$ (rad^{-1})	0	0	-0.05	0
$C_{l\beta}$ (rad^{-1})	-0.17	-0.17	-0.17	-0.17
$C_{n\beta}$ (rad^{-1})	-1.3E-2	-9.4E-3	-1.1E-2	-1.3E-2
C_{lp} (rad^{-1})	-0.94	-0.94	-0.945	-0.954
C_{np} (rad^{-1})	-0.16	-0.16	-0.16	-0.16
C_{lr} (rad^{-1})	0.40	0.40	0.40	0.40
C_{nr} (rad^{-1})	-0.0127	-0.0143	-0.0134	-0.0125
$C_{n\delta r}$ (rad^{-1})	-1.4E-2	-1.5E-2	-1.5E-2	-1.4E-2
δ_e ($^\circ$)	0.3	0.29	0.12	-0.06
δ_r ($^\circ$)	0	0	-0.23	0

Longitudinally, the rotation of sail tails brings little effect on aerodynamic efficiency at small angles of attack in equilibrium. However, the aerodynamic center moves backwards when rotation-deviation angles are gradually close to 0° , resulting moderate increasing of longitudinal static and dynamic stability. Laterally, static directional stability denoted as $C_{n\beta}$ and yawing-directional damping increases of slight degree when rotation-deviation angle closer to $\pm 90^\circ$, while the installation and rotation of sail tails bring little effect on roll stability derivatives. Particularly, when the rotation-deviation angle of sail tails is not equal to 0° or $\pm 90^\circ$, coupling between longitudinal and lateral-directional derivatives was of slight degree, and three of cross-coupling derivatives are bold in Table 4. It brings control law complexity. In addition, deflection of each elevator and rudder used for trim is little and differs of slight degree for

different configurations. In conclusion, the influence brought by the installation and rotation of sail tails is slight, though the area ratio of sail tails to the wing is considerable. It is because that the aspect ratio of sail tails, expressed by b_v/c_t , is equal to 0.19, which results in so small normal forces that generated moments are of slight degree. When five sail sails are united as one sail tail with the aspect ratio of about 1.0, it is further investigated that its influence of installation and rotation of the sail tails augment significantly on stability and control, and most of them are negative. From this point of view, tracking sails divided into several equal units with span-loader guideline can moderate the influence rotating sail tails on stability and control of the wing-sail configuration.

9 Conclusion

A design methodology of year-round solar-powered stratospheric UAVs at low to middle latitudes is developed, which can be equally applied to configurations with or without non-horizontal sun-trackers. The configurations are generally categorized into the conventional type and the wing-sail type. Based on traditional design methodology, the proposed methodology comprehensively comprises formulations for power absorption of PV modules, each mass component, and aerodynamic efficiency. Particularly, the thermodynamics and orientations of PV modules at all latitudes and stratospheric altitudes throughout a whole year are considered. Besides, the QPSO algorithm and Kriging surrogate model are integrated into the methodology in order to obtain a group of optimal conceptual parameters effectively. It is applied for comparative analysis on both configurations and a conceptual design of wing-sail configuration. The applications demonstrate the utility of the design methodology.

In the comparative analysis, the wing-sail significantly outperforms the conventional at middle latitudes for year-round operation in the aspects of dimensions, total area of PV modules needed, cruise velocity, payload capability. At low latitudes, the conventional and the wing-sail are both suitable for year-round operation and

the latter does not show much superiority over the former.

In view of limited investigations on year-round operational potentials at middle latitudes only by solar energy, a wing-sail concept named PoXiao is developed by the design methodology at the latitude of 45°N, and its energy performance at middle latitudes and characteristics of stability and control influenced by tracking sail tails are also investigated preliminarily. From an energy point of view, the winter solstice acts as the critical design condition at middle latitudes in the northern hemisphere. During year-round operation, it is practicable to increase station-keeping altitude or augment payload power consumption to enhance the mission capability in the period from spring to autumn when solar energy absorption is surplus. In addition, the addition and rotation of sail tails of PoXiao have slight influence on the characteristics of stability and control, and the degree of influence will increase if the aspect ratio of sail tails increase.

Future research work will focus on four aspects, mainly for the wing-sail configuration. Firstly, the tracking method for sail tails is not limited on Azimuth-Elevation tracking method. Further investigations will be focused on sensitivity analyses of conceptual parameters to explore flight principles of the wing-sail configuration with different kinds of tracking methods. Secondly, if the gravimetric energy density of secondary batteries is not higher enough, a portion of the diurnal surplus of solar energy by tracking sails can be stored in potential energy by gaining a certain altitude. The guideline will be incorporated into the methodology. Thirdly, longitudinal and lateral dynamic modes relative to the addition and rotation of sail tails will be further investigated and flight simulations will be carried out in real time especially during the Azimuth tracking or Elevation tracking. Finally, the nonlinear flight dynamics of the span-loader configuration with or without sail tails will be investigated.

References

- [1] P.B. MacCready, P.B.S. Lissaman, W.R. Morgan, J.D. Burke. "Sun-Powered Aircraft Designs,"

- JOURNAL OF AIRCRAFT, Vol. 20, No. 6, 1983, pp.487-493.
- [2] Robert J. Boucher. "Sunrise, the World's First Solar-Powered Airplane," JOURNAL OF AIRCRAFT, Vol. 22, No. 10, 1984, pp.840-846.
- [3] Patrick Berry. "The Sunriser - A Design Study in Solar Powered Flight," AIAA Paper 2000-01-5507, 2000.
- [4] M.D. Bailey, M.V. Bower. "High Altitude Solar Power Platform," NASA TM-103578, 1992.
- [5] Steven A. Brandt, Fred T. Gilliam. "Design Analysis Methodology for Solar-Powered Aircraft," JOURNAL OF AIRCRAFT, Vol. 32, No. 4, 1995, pp.703-709.
- [6] Giulio Romeo, Giacomo Frulla, Enrico Cestino, Guido Corsino. "HELIPLAT: Design, Aerodynamic, Structural Analysis of Long-Endurance Solar-Powered Stratospheric Platform," JOURNAL OF AIRCRAFT, Vol. 40, No. 6, 2004, pp.1505-1520.
- [7] G. Romeo, G. Frulla, E. Cestino. "Design of a High-Altitude Long-Endurance Solar-Powered Unmanned Air Vehicle for Multi-Payload and Operations," Journal of Aerospace Engineering, Vol. 221, No. 119, 2007, pp.199-216.
- [8] André NOTH. "Design of Solar Powered Airplanes for Continuous Flight," Ph.D. Dissertation, Ecole Polytechnique Fédérale de Lausanne, ETH ZÜRICH, Switzerland, 2008.
- [9] E. Rizzo, A. Frediani. "A Model for Solar Powered Aircraft Preliminary Design," THE AERONAUTICAL JOURNAL, Vol. 112, No. 1128, 2008, pp.57-78.
- [10] Thomas E. Noll, John M. Brown, Marla E. Perez-Davis, Stephen D. Ishmael, Geary C. Tiffany, Matthew Gaier. "Investigation of the Helios Prototype Aircraft Mishap," NASA Report, Jan. 2004.
- [11] John A. Duffie, William A. Bechman, Solar Engineering of Thermal Processes, 3rd ed., JOHN WILEY & SONS, New Jersey, 2006.
- [12] Min Chang, Zhou Zhou, Yingying Li. "An Effective Theoretical Analysis of Persistent Flight Altitudes of Solar-Powered Airplanes," Journal of Northwestern Polytechnical University, Vol. No. 2012.
- [13] B. Keidel. "Auslegung und Simulation von Hochfliegenden Dauerhaft Stationierbaren Solardrohnen," Ph.D. Dissertation, Fakultät für Maschinenwesen, Technischen Universität München, München, 2000.
- [14] Gerald D. Miller, United States Patent for a "Solar Powered Aerial Vehicle". filed 25 Jul. 2007.
- [15] Chang M, Zhou Z, Cheng K, Wang R. "Exploring the Characteristics of Power Density of Tracking PV Modules for High-Altitude Stationary Solar-Powered Airplanes," Acta Aeronautica et Astronautica Sinica, Vol. 34, No. 2, 2013, pp.273-281.
- [16] Søren N. Lophaven, Hans Bruun Nielsen, Jacob Søndergaard. "DACE - A Matlab Kriging Toolbox," Technical Report IMM-TR-2002-12, 2002.
- [17] Jun Sun, Wenbo Xu, Bin Feng, "A Global Search Strategy of Quantum-Behaved Particle Swarm Optimization," Proceedings of the 2004 IEEE Conference on Cybernetics and Intelligent Systems, Singapore, 1-3 December, 2004.
- [18] D. Hall, C. Fortenbach, E. Dimiceli, R. Parks. "A Preliminary Study of Solar Powered Aircraft and Associated Power Trains," NASA CR-3699, 1983.
- [19] Durisch W., Urban J., Smestad G. "Characterisation of Solar Cells and Modules Under Actual Operating Conditions," Renewable Energy, Vol. 8, No. 1-4, 1996, pp.359-366.
- [20] D.A. Scheiman, P.P. Jenkins, D.J. Brinker, J. Appelbaum, "Low Intensity Low Temperature (LILT) Measurements and Coefficients on New Photovoltaic Structures," Progress in Photovoltaics: Research and Applications, Vol.4: John Wiley and Sons, Inc., 1996.
- [21] Incropera Frank P., David P. Dewitt, Fundamentals of Heat and Mass Transfer, 7th ed., John Wiley & Sons, New York, 2011.
- [22] Terry D. Haws, W. Jerry Bowman. "Thermal Analysis of the Pathfinder Aircraft " AIAA 99-0735, 1999.
- [23] Xiaojian Li, Xiande Fang, Qiuming Dai. "Research on Thermal Characteristics of Photovoltaic Array of Stratospheric Airship," JOURNAL OF AIRCRAFT, Vol. 48, No. 4, 2011, pp.1380-1386.
- [24] Stuart F. Brown. "The Eternal Airplane," Popular Science, Vol. 244, No. 4, 1994, pp.70-75.
- [25] P.G. Carey, R.C. Aceves, N.J. Colella, K. A. Williams, R.A. Sinton, G.S. Glenn. "A Solar Module Fabrication Process for HALE Solar Electric UAVs," UCRL-JC--118267, 1994.
- [26] Ron Laurenzo. "Soaring on a Solar Impulse," AEROSPACE AMERICA, Vol. No. 2009, pp.32-36.
- [27] Daniel P. Raymer, Aircraft Design: A Conceptual Approach, 4th ed., American Institute of Aeronautics and Astronautics, Inc., Washington D.C., 1999.
- [28] Sivells J. C., Neely R. H. "Method for Calculating Wing Characteristics by Lifting-Line Theory Using Nonlinear Section Lift Data," NACA Rept. 865, 1947.
- [29] M. Drela, "XFOIL: An Analysis and Design System for Low Reynolds Number Airfoils," Conference on Low Reynolds Number Airfoil Aerodynamics, University of Notre Dame, 1989.
- [30] James Kennedy, Russell Eberhart, "Particle Swarm Optimization," Proceedings of the Fourth IEEE International Conference on Neural Networks, Perth, Australia, 1995: 1942-1948.
- [31] Sun Meijian, Zhan Hao. "Synthesis Airfoil Optimization by Particle Swarm Optimization Based on Global Information," Acta Aeronautica et Astronautica Sinica, Vol. 31, No. 11, 2010, pp.2166-2173.
- [32] G.Venter, J. Sobieszczanski Sobieski. "Multidisciplinary Optimization of a Transport Aircraft Wing Using Particle Swarm optimization," Structural and Multidisciplinary Optimization, Vol. 26, No. 1-2, 2004, pp.121-131.
- [33] L. Blasi, G. Del Core. "Particle Swarm Approach in Finding Optimum Aircraft Configuration,"

JOURNAL OF AIRCRAFT, Vol. 44, No. 2, 2007,
pp.679-682.

- [34] Jun Sun, Bin Feng, Wenbo Xu, "Particle Swarm Optimization with Particles Having Quantum Behavior," IEEE Proceeding of Congress on Evolutionary Computation, 2004: 325-331.

Contact Author Email Address

Contact author: Min Chang
Email: Changmin0806@163.com

Copyright Statement

The authors confirm that they, and/or their company or organization, hold copyright on all of the original material included in this paper. The authors also confirm that they have obtained permission, from the copyright holder of any third party material included in this paper, to publish it as part of their paper. The authors confirm that they give permission, or have obtained permission from the copyright holder of this paper, for the publication and distribution of this paper as part of the ICAS 2014 proceedings or as individual off-prints from the proceedings.